SCIENTIFIC REPORTS

OPEN

SUBJECT AREAS:
NANOPHOTONICS AND PLASMONICS
NANOSCALE MATERIALS

Received
11 August 2014

Accepted
8 December 2014

Published
12 January 2015

Correspondence and requests for materials should be addressed to X.F. (xshfang@fudan.edu.cn)

Hexagonal-like Nb_2O_5 Nanoplates-Based Photodetectors and Photocatalyst with High Performances

Hui Liu[1], Nan Gao[1], Meiyong Liao[2] & Xiaosheng Fang[1]

[1]Department of Materials Science, Fudan University, Shanghai 200433, P. R. China, [2]Optical and Electronic Materials Unit, National Institute for Materials Science (NIMS) Namiki 1-1, Tsukuba, Ibaraki 305-0044, Japan.

Ultraviolet (UV) photodetectors are important tools in the fields of optical imaging, environmental monitoring, and air and water sterilization, as well as flame sensing and early rocket plume detection. Herein, hexagonal-like Nb_2O_5 nanoplates are synthesized using a facile solvothermal method. UV photodetectors based on single Nb_2O_5 nanoplates are constructed and the optoelectronic properties have been probed. The photodetectors show remarkable sensitivity with a high external quantum efficiency (EQE) of 9617%, and adequate wavelength selectivity with respect to UV-A light. In addition, the photodetectors exhibit robust stability and strong dependence of photocurrent on light intensity. Also, a low-cost drop-casting method is used to fabricate photodetectors based on Nb_2O_5 nanoplate film, which exhibit singular thermal stability. Moreover, the hexagonal-like Nb_2O_5 nanoplates show significantly better photocatalytic performances in decomposing Methylene-blue and Rhdamine B dyes than commercial Nb_2O_5.

Two dimensional (2D) nanostructures have attracted increasing attention due to the unique nanoscale phenomena and their potentials in many areas ranging from energy storage to environmental protection[1]. Compared with one dimensional (1D) and zero dimensional (0D) nanostructures, 2D nanostructures show great advantages in some special applications. It has been theoretically and experimentally demonstrated that some 2D nanostructures of noble metals or upconversion materials have higher optical activities, and the related properties can even be precisely tuned by controlling the 2D morphologies[2–4]. Further to that, ZnO nanoplates with a high population of polar Zn (0001) faces show higher photocatalytic activity in H_2O_2 generation, compared with ZnO nanorods[5]. Nanoplates of SnS_2[6], $LiCoPO_4$[7], and carbon-coated $LiFePO_4$[8] exhibit superior capacities for Lithium ion batteries. Also, 2D nanostructures with highly faceted planes are favorable for self-assembling into desired 2D or 3D patterns, and further for the production of complex nanoscale architectures useful for practical applications, such as solar cells and plasmonic metamaterials[9,10]. In addition, it has been reported that the nanomaterials from single-component systems or nanoplate mixtures with sulphur-doped pnictogen chalcogenide exhibit higher figure of merit in thermoelectricity than their bulk counterparts[11,12].

Niobium pentaoxide (Nb_2O_5), one of the most influential inorganic semiconductors, is known for its dielectric strength and effectiveness in catalysis[13–17]. Up to now, various interesting morphologies of Nb_2O_5 nanostructures, such as nanowires[18], nanobelts[19], nanorods[20], nanotubes[21,22], opal nanostructure[23], mesoporous[24,25], hollow nanospheres[26], nanosheets[27], and nanoparticles[28], have been synthesized. These nanostructures offer Nb_2O_5 several unique features for a variety of device applications, involving field emitters[29], lithium ion batteries[30], photodetectors[31], photocatalyst[32], biosensors[33], gas sensors[34], etc. Owing to its bandgap, which rests in a relatively wide range from about 2.8 to 3.8 eV depending on the preparation methods[35–37], Nb_2O_5 is a potential candidate for UV-A light (wavelengths ranging from 400 nm to 320 nm) detection. However, until now, studies of the UV-A light photodetectors based on Nb_2O_5 nanostructures have been rather limited, compared with those based on the nanostructures of ZnO[38], ZnS[39], and SnO_2[40]. In fact, although the photodetectors based on single Nb_2O_5 nanobelts[31] and hollow nanospheres[41] were reported, the time response performances were not satisfactorily resolved. Furthermore, the synthesis of both nanostructures needs a complicated template-assisted process. The photodetectors based on single Nb_2O_5 nanowires were also reported[42]. Nevertheless, the studied response wavelengths of the nanowire were 808 nm (~1.5 eV) and 532 nm (~2.3 eV), which were deduced to result from the defect level states of nanowire. This means the corresponding photon energy is much lower than the bandgap, and therefore, these Nb_2O_5 nanowires cannot be used as UV-A photodetectors. In this work, by using a facile one pot

solvothermal method, we synthesize hexagonal-like Nb_2O_5 nanoplates without using any templates or surfactants, and, based on the as-prepared samples, fabricate UV-A photodetectors. The temperature-dependent current-voltage characteristics of the photodetector made from Nb_2O_5 nanoplate film using a low-cost drop-casting method are analyzed. It is demonstrated that the resulted photodetectors based on Nb_2O_5 nanoplates exhibit remarkable selectivity, thermal stability, and sensitivity with a high EQE. Furthermore, the as-obtained products also show significantly better photocatalytic performances than commercial Nb_2O_5.

Results

Characterization of Nb_2O_5 samples. From the low and high resolution field emission scanning electron microscopy (SEM) images of Fig. 1a–c, it is noticed that the as-prepared samples mainly display hexagonal-like nanoplate morphologies, with typical diameters ranging from 0.5 to 2 μm and thickness around 100 nm. Statistical analysis shows the nanoplates take a significant percentage ($>$ 80%) of the yield, which is interspersed with a few nanorods about 1.5 μm long and a few nanoparticles. Powdered X-ray diffraction (XRD) pattern of the as-obtained samples is shown in Fig. 1d. All diffraction peaks are indexed to the hexagonal Nb_2O_5 (PDF#07-0061) phase and monoclinic Nb_2O_5 (PDF#19-0862) phase and no impurities are observed. Transmission electron microscopy (TEM) and selected area electron diffraction (SAED) have been performed to further confirm the morphology and structure. Fig. 2a shows the TEM image of the nanoplates, which substantiates the hexagonal-like morphology. The SAED pattern taken of individual Nb_2O_5 nanoplates can be indexed to the [001] zone axis, exhibiting a hexagonally arranged diffraction spot, as shown in Fig. 2b. This is consistent with the XRD result that the hexagonal phase is formed in the as-prepared sample. Also, to confirm the chemical composition and elemental distribution, X-ray dispersive spectroscopy (EDS) has been conducted on the hexagonal-like nanoplates, as shown in Fig. 2c–e. The results indicate that the samples only consist of Nb and O elements with a stoichiometric $Nb_2O_{4.8}$ composition, where the Cu signal originates from the TEM copper grid. The mapping images in Fig. 2c and 2d show that they are homogeneously distributed within the nanoplates. Besides, high resolution transmission electron microscopy (HRTEM) image and SAED pattern are shown in Fig. S1, consistent with the XRD result that the nanorods exhibit a monoclinic Nb_2O_5 phase. The EDS elemental mapping images of both hexagonal-like nanoplates and nanorods also confirm the uniform distribution of Nb and O in the nanorods. Further to that, additional analysis using X-ray photoelectron spectroscopy (XPS) has been performed and shown in Fig. 3. XPS survey scan implies that only Nb and O elements are present in the sample, apart from some residual carbon signal which is believed to arise from adventitious contamination (Fig. 3a). However, the Nb peak can be deconvoluted into two peaks with binding energies of 207.2 eV and 205.8 eV, and are assigned to Nb^{5+} and Nb^{4+}, respectively. This agrees well with the reported literature values (207.0 to 207.6 eV for Nb 3d5/2 in Nb_2O_5 and 205.2 to 206.1 eV for Nb 3d5/2 in NbO_2 according to the NIST database)[32,43]. Furthermore, these results also suggest that there are small amounts of suboxide species such as NbO_2 in the Nb_2O_5, in accordance with the EDS stoichiometric $Nb_2O_{4.8}$ composition.

Discussion

The single hexagonal-like nanoplate photodetector was fabricated according to the experimental section. The schematic illustration of the single nanoplate-based photodetector and a typical SEM image are shown in Fig. 4a and 4b, respectively. It is noticed that the gap between the two electrodes is about 1.3 μm. The optoelectronic properties of the nanoplate-based photodetector are measured using a two-probe method under ambient conditions. Fig. 4c displays the typical current-voltage (I-V) curves of the device either illuminated with light of different wavelengths or in dark conditions. The device has shown a very low dark current of less than 1 pA under the bias

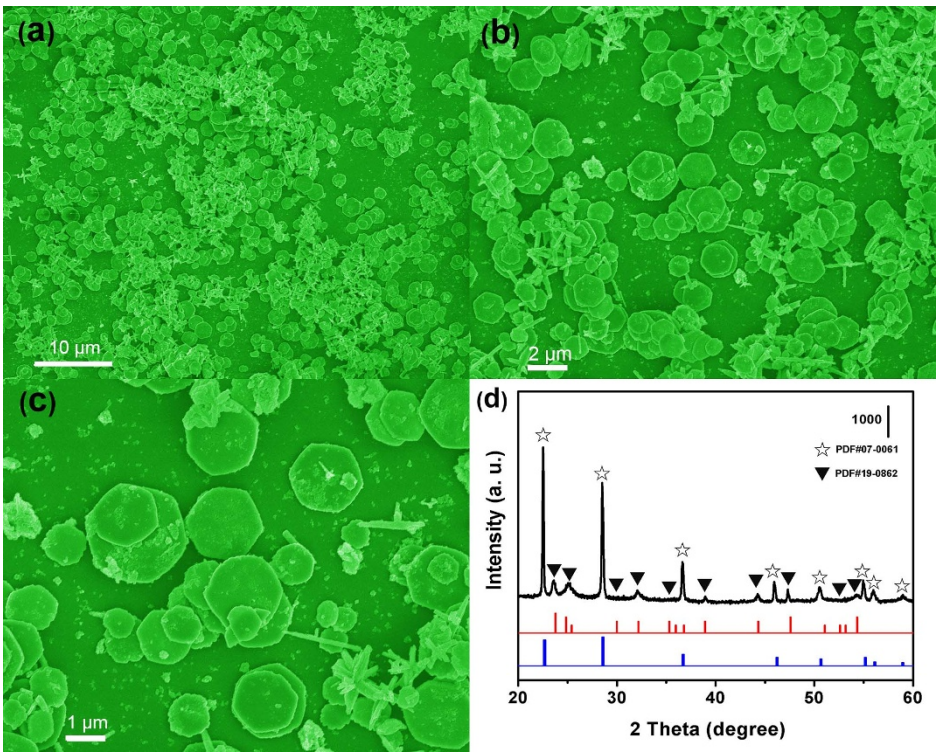

Figure 1 | Nb_2O_5 sample synthesized through a solvothermal method. (a) – (c) Low and high magnification SEM images of hexagonal-like nanoplates. (d) XRD pattern of the obtained Nb_2O_5.

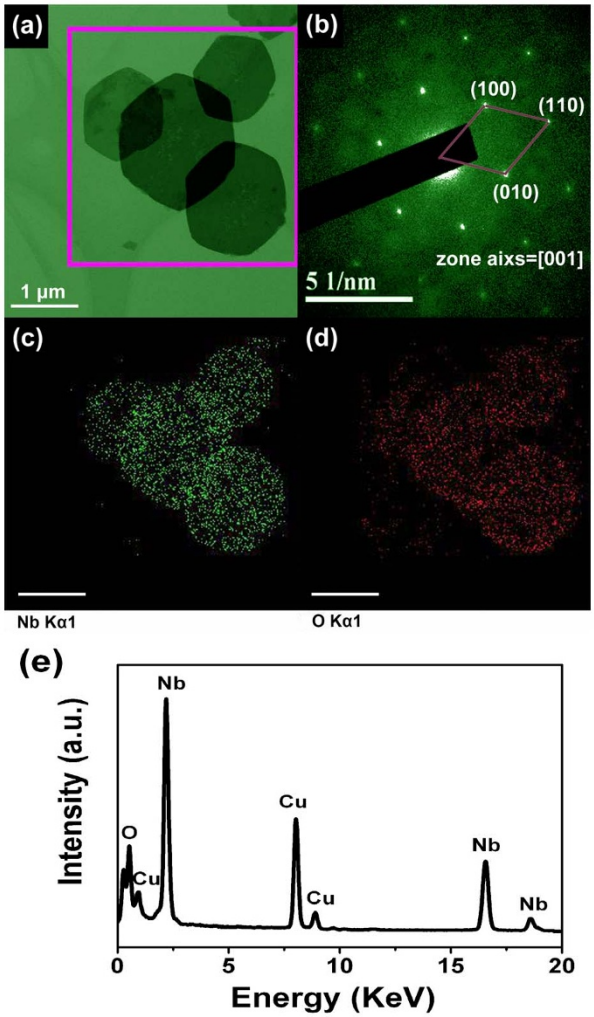

Figure 2 | Nb_2O_5 sample synthesized through a solvothermal method. (a) TEM image of hexagonal-like nanoplates. (b) SAED pattern of a single nanoplate Nb_2O_5. The corresponding EDS mapping images for Nb and O of the hexagonal-like nanoplates marked in the rectangle area in (a) are shown in (c) and (d), respectively. (e) EDS spectrum.

voltage of 1.0 V. When the wavelength of the light source is 450 nm, there is almost no change in photocurrent, which fairly overlaps with the curve of the dark current. However, when the device is illuminated by the light with shorter wavelengths, for example of 350 nm and 320 nm, the photocurrent increases drastically and reaches up to 36.5 pA and 59.9 pA, respectively. This indicates that the present Nb_2O_5 nanoplate-based photodetector is significantly more sensitive to UV-A light than to visible light. The nonlinear behaviors of *I-V* curves may be caused by the blocking at the metal/semiconductor contacts. In fact, the almost rectifying *I-V* characteristic of the present device can be ascribed to the metal-semiconductor-metal structure involving two Schottky barriers connected back to back and a resistor in between, where the current in the nano-Schottky barrier structure becomes dominant and has greater tendency to become tunneling rather than thermionic[44,45]. The dramatic increase in photocurrent under 350 nm and 320 nm light illuminations is ascribed to the enhanced numbers of excited electron-hole pairs when the photons' energy is larger than the bandgap of Nb_2O_5. This high wavelength selectivity is also confirmed by the spectral photoresponses of the device under a bias of 1.0 V against wavelengths ranged from 630 nm to 250 nm, where stronger absorption occurs under the wavelengths below 400 nm, as shown in Fig. 4d. The bandgap is deduced from the UV-vis absorption spectrum, as shown in Fig. 4e and 4f. As for direct bandgap semiconductors, it is known that the relationship between absorption coefficient (α) near the absorption edge and the optical bandgap obeys the following equation[46,47]:

$$(\alpha h\nu)^2 = \mathrm{A}(h\nu - \mathrm{Eg})$$

where A is the absorption constant that relates to the effective masses associated with the valence and conduction bands, and $h\nu$ is the photon energy. Hence, the optical bandgap for the absorption edge can be obtained by extrapolating the linear portion of the plot of $(\alpha h\nu)^2$ against $h\nu$ down to the point where $\alpha = 0$. Fig. 4f shows the plot of $(\alpha h\nu)^2$ against $h\nu$ calculated from Fig. 4e. It is noticed that the optical absorption in the edge region fits well with the relation of $(\alpha h\nu)^2 \propto (h\nu\text{-Eg})$, which indicates that the Nb_2O_5 sample have a direct bandgap of 3.15 eV (393 nm). This relatively low value of bandgap is consistent with the results of Nb_2O_5 samples synthesized using sol-gel methods at low temperatures, while it is reported that Nb_2O_5 samples made by evaporation, sputtering, anodization and CVD have higher values of bandgap[35–37].

Responsivity (R_λ) and EQE are two critical parameters to determine the sensitivity of a photodetector, and they are defined as the number of carriers circulating through a photodetector per absorbed photon and per unit time, respectively[48]. A larger R_λ or EQE means a higher sensitivity, and they can be expressed as $R_\lambda = \Delta I/PS$ and EQE $= R_\lambda hc/e\lambda$, respectively, where ΔI is the difference between the photocurrent and the dark current, P is the light power, S is the irradiated area on the nanoplate, h is Planck's constant, c is the velocity of light, e is the electronic charge, and λ is the excitation wavelength. The calculated R_λ and EQE of the present nanoplate device are as high as 24.7 A/W and 9617% under an applied voltage of 1 V, respectively, when the illumination wavelength is 320 nm (134 μW/cm^2).

Apart from sensitivity and selectivity, stability is also a very important factor for photodetectors. Fig. 5a and 5b show the time-dependent responses of the photodetector, which are obtained either using or without using the mechanical chopping method upon the illumination of 320 nm light, under a bias of 1.0 V. When the condition is changed from dark to light, the current increases to a stable

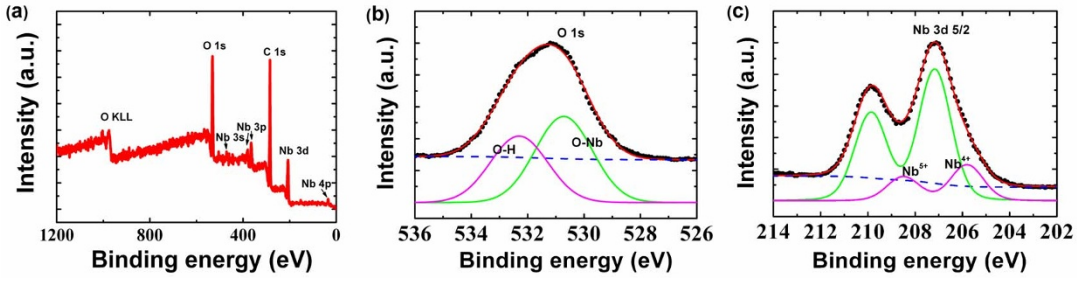

Figure 3 | Nb_2O_5 sample synthesized through a solvothermal method. (a) XPS survey scan of Nb_2O_5 samples. (b) and (c) high resolution XPS spectra for O and Nb.

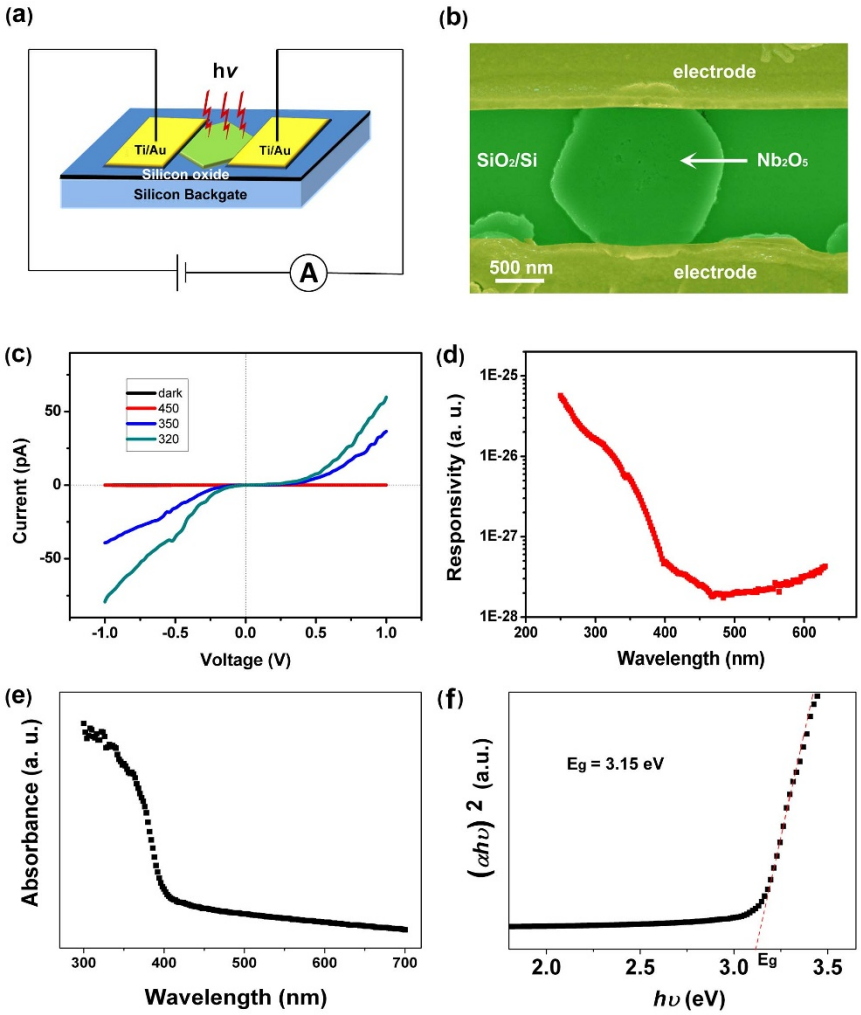

Figure 4 | Device illustration, spectral and optoelectronic characteristics of single nanoplate photodetector. (a) Schematic illustration and (b) SEM image of a Nb_2O_5 nanoplate photodetector. (c) *I-V* characteristics of the single-nanoplate photodetector, either illuminated with light at three different wavelengths or kept in dark conditions, under a bias of 1.0 V. (d) Spectral photoresponses of the nanoplate photodetector against a series of wavelengths ranged from 630 nm to 250 nm measured under the bias of 1.0 V. (e) UV-vis absorption spectrum. (f) The plot of $(\alpha hv)^2$ against hv for the Nb_2O_5 sample, where Eg is the optical bandgap.

value around 55 pA, and, after the light is turned off, decreases dramatically to the original value of less than 1 pA, as shown in Fig. 5a. The rise time and decay time (defined as the time required for the peak photocurrent to increase from 10% to 90% or drop from 90% to 10%) of the present photodetector are 28 s and 12 s, respectively. Furthermore, upon constant illumination, the photocurrent fluctuates very little and no obvious degradation is observed for the average photocurrent of ~ 55 pA over 1400 s. These critical parameters from the measurements are comparable to those of some other existing semiconductor photodetectors listed in Table S1 in the Supplementary Information. Compared with individual Nb_2O_5 nanobelt UV-A photodetector, the present single nanoplate photodetector exhibit a stable time response and higher respnosivity. Fig. 5c shows the variation of photocurrent generated by the photodetector against light intensity upon illumination of the 320 nm light under the bias of 1.0 V. The photocurrent increases with light intensity, consistent with the fact that the amount of photo-generated charge carriers is proportional to the absorbed photon flux. The best-fit relationship between photocurrent and light intensity obeys the power law, $I \sim P^{0.74}$; the exponent is very close to that of the three-quarter power law, implying that the present device may suffer from space charge limited effects[49].

The efficiency of photocurrent generation depends on the balance among charge carriers generation, recombination, and transport[49]. It is generally accepted that chemisorption/desorption of oxygen molecules plays a very important role in regulating the photoconductive process in semiconductors. Due to the large surface-to-volume ratio of the Nb_2O_5 nanoplates resulting from its hexagonal-like geometry with the width of 0.5 to 2 μm and the thickness around 100 nm, chemisorption/desorption on the surface of Nb_2O_5 nanoplates may also plays a fairly important role in the photoconductive behaviors, as previously reported of Nb_2O_5 nanobelts[31]. Therefore, we investigate the *I-V* characteristics of Nb_2O_5 nanoplate photodetector upon the 320 nm illumination in air and vacuum, as shown in Fig. 5d. The photocurrent measured under the pressure of 100 Pa is 454 pA, which is about 7.5 times higher than that in air (59.9 pA). This phenomenon is ascribed to the reason same to that for the previously reported Nb_2O_5 nanobelts[31]. Because Nb_2O_5 is an n-type semiconductor, oxygen molecules are absorbed onto the surface and then capture the free electron of the nanoplate through the reaction $[O_2(g) + e^- \rightarrow O_2^-(ad)]$ at ambient conditions, giving rise to a low-conductivity depletion layer and the band bending near the surface. Upon UV illumination, electron-hole pairs are generated and the holes will migrate to the surface, leading to the desorption of oxygen

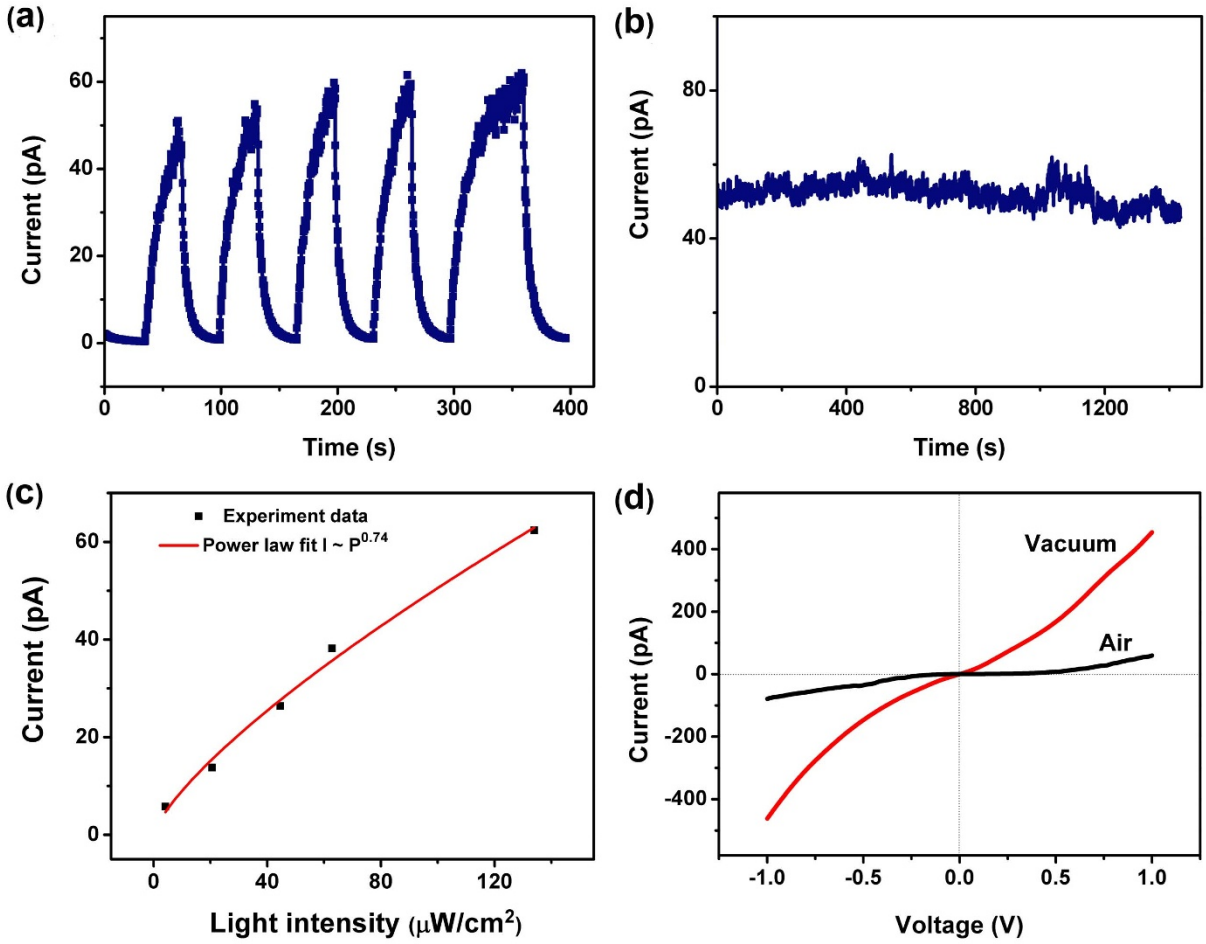

Figure 5 | Photoresponse of single nanoplate photodetector. (a) and (b) Time-dependent responses of the photodetector upon illumination of the 320 nm light measured using the mechanical chopping method (a) and without using the mechanical chopping method (b) under the bias of 1.0 V. (c) Variation of the photocurrent generated by the photodetector under the bias of 1.0 V against light intensity upon illumination of the 320 nm light. (d) *I-V* characteristics upon illumination of the 320 nm light in air and vacuum, respectively.

molecules from the nanoplate surface, expressed as $[h^+ + O_2^-(ad) \rightarrow O_2(g)]$. Thus, the photo-induced electrons will lead to an apparent enhancement of photocurrent in air. In vacuum, more adsorbed oxygen molecules are desorbed from the surface, hence bringing up a higher photocurrent than that in air. This is consistent with previous reports of an enhancement of both photocurrent and photoluminescence in vacuum[50–52].

In a bid to explore both the probability of low-cost manufacturing and the thermal stability of photodetectors, Nb_2O_5 nanoplate film has been prepared by using the drop-casting method on SiO_2/Si substrates. Tungsten carbide (WC) electrodes (50 nm) were utilized for higher temperature measurement, and patterned, using a hard mask with 20 μm gaps, as shown in Fig. 6a. All measurements performed were similar to those for the single-nanoplate photodetector. *I-V* and current-time characteristics are shown in Fig. 6b and 6c. The linear behaviors of *I-V* curves suggest good Ohmic contacts between the nanoplates and the electrodes. The responses of current under different wavelengths show the same trend to that of the single Nb_2O_5 nanoplate photodetector, where the photocurrent changes obviously upon the 350 nm and 320 nm illuminations. The current steadily changes as the light is turned on and off, as shown in Fig. 7a. However, the current-time responses in vacuum in Fig. 7b display a gradual increase of both photocurrent and dark current, which is attributed to the reduction in oxygen reabsorption rate in oxygen-deficient environments[53]. The changes in photocurrent under the bias of 1.0 V upon 320 nm illumination in air or vacuum at different temperatures are summarized in Table S2 in Supporting Information. It can be seen that the photocurrent of the Nb_2O_5 nanoplate film photodetector is about only one third of that of the single Nb_2O_5 nanoplate photodetector. The possible reason for this large difference in photocurrent is that shorter gap distances may result in shorter time for the carriers to transit through the gap, and thus higher photocurrent[53]. Besides, when the temperature increases from 298 K to 358 K, both the photocurrent and the dark current, as well as the responsivity, are only slightly increased, indicating good thermal stability of the Nb_2O_5 nanoplate film photodetector and great potential for the photodetector to work efficiently at higher temperatures.

Apart from being used as a photodetector, the Nb_2O_5 nanoplates are also testified of its semiconductor property to decompose Methylene-blue and Rhodamine B. The concentrations of these two dyes are determined based on Beer's law, and the absorbance of 664 nm and 554 nm is investigated, respectively[54]. From Fig. 8, it is noticed that the as-prepared Nb_2O_5 nanoplates show a faster decomposition rate than commercial Nb_2O_5 (Aladdin, 99.99%, particles, several μm in diameter, Fig. S2) of these two dyes. The appearance of a new peak around 495 nm in Fig. 8d, after 40 minutes' irradiation, is assigned to rhodamine (the full N-deethylated products of Rhodamine B)[55,56]. The absorbance changes are also summarized in Table S3. It is clear that nearly 91% and 99% of the initial dyes still remain in the solution after 60 minutes of irradiation without any photocatalyst. The Nb_2O_5 nanoplates show a higher adsorp-

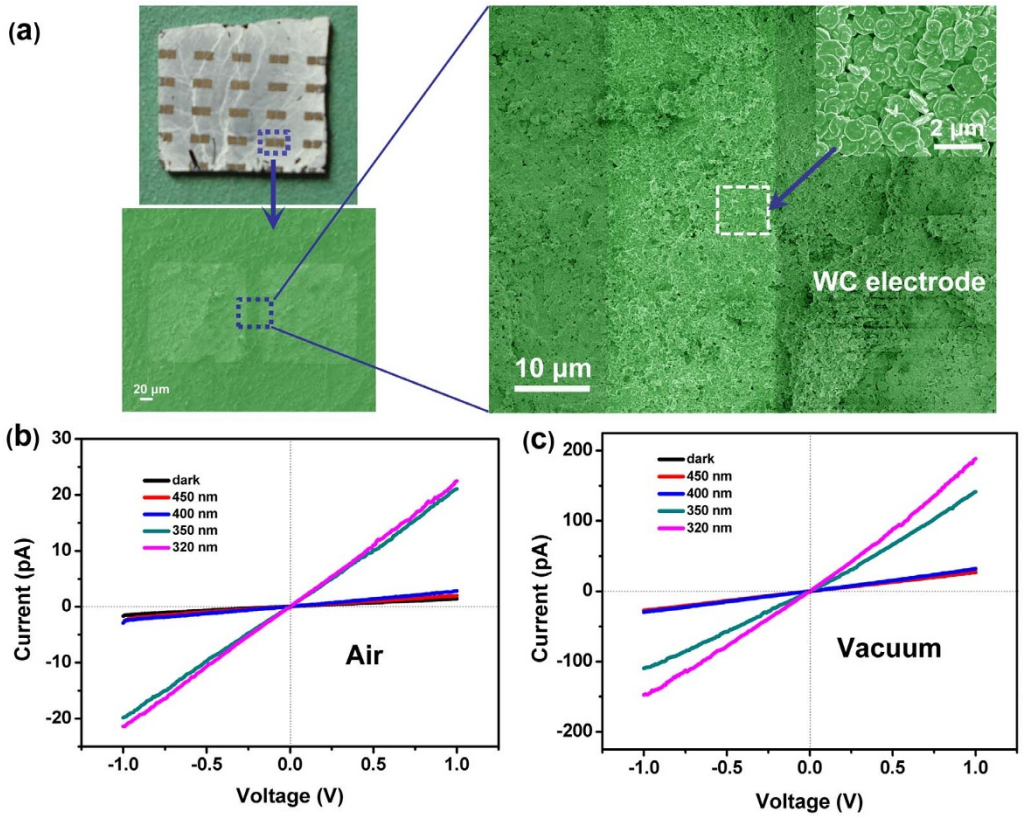

Figure 6 | Device image and optoelectronic characteristics of nanoplate film photodetector. (a) Photograph and SEM images of the nanoplate film photodetector produced using the drop-casting method. (b) and (c) *I-V* characteristics of the device illuminated with light under four different wavelengths and in dark conditions under the bias of 1.0 V, in air and vacuum, respectively.

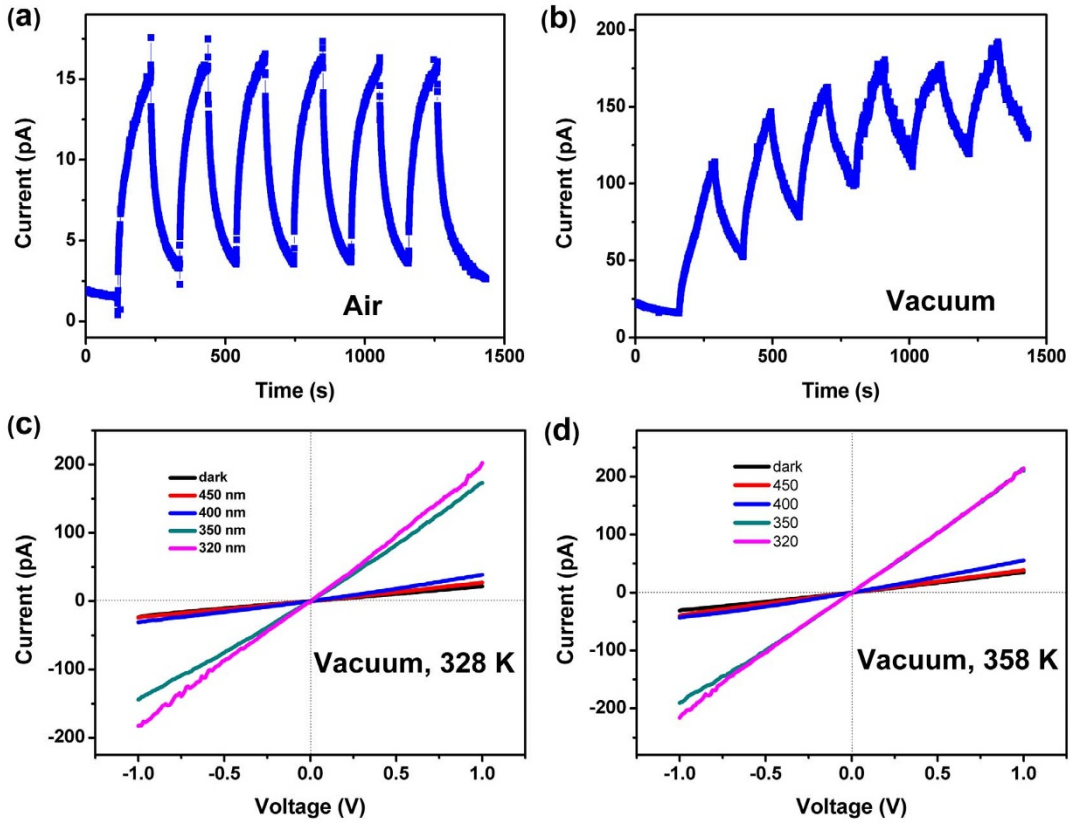

Figure 7 | Photoresponse and temperature dependence of nanoplate film photodetector. (a) and (b) Current-time responses of the nanoplate film photodetector illuminated upon the 320 nm light measured using the mechanical chopping method under the bias of 1.0 V in air and vacuum, respectively. (c) and (d) *I-V* characteristics of the device, under the temperatures of 328 K and 358 K, respectively, in vacuum.

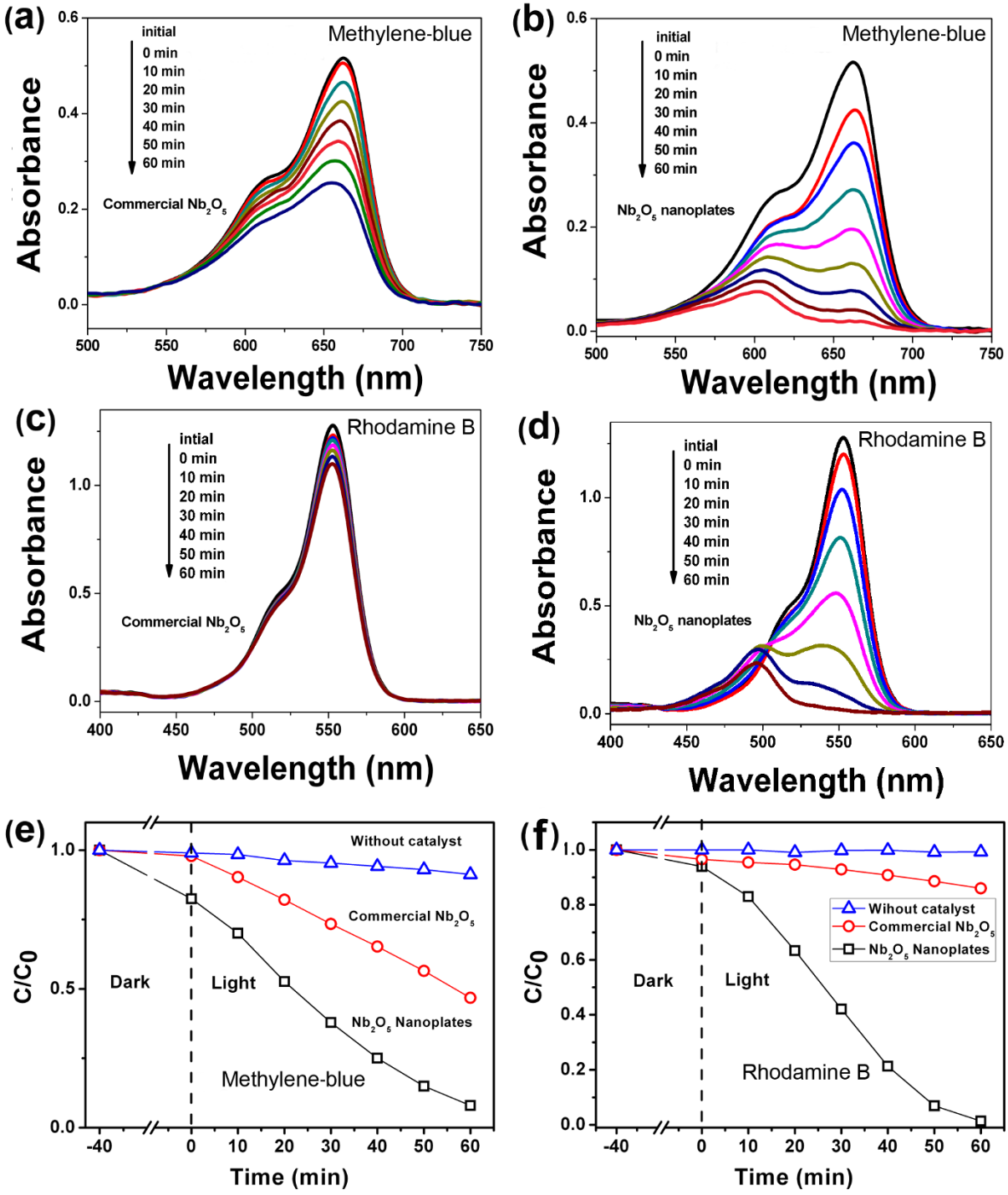

Figure 8 | Photocatalytic performances of Nb_2O_5. (a) and (b) Absorbance changes of Methylene-blue in the presence of commercial Nb_2O_5 and as-prepared Nb_2O_5 nanoplates. (c) and (d) Absorbance changes of Rhodamine B in the presence of commercial Nb_2O_5 and as-prepared Nb_2O_5 nanoplates. (e) and (f) Comparison of Methylene-blue and Rhodamine B decomposition efficiencies between the solutions with as-prepared Nb_2O_5 nanoplates, the solutions with commercial Nb_2O_5 and the solutions without catalyst, respectively.

tion and decomposition ratio of dye molecules than commercial Nb_2O_5 (The absorbance changes from 92% at 0 minute to 54% at 60 minute for Methylene-blue, and from 98% at 0 minute to 14% at 60 minute for Rhodamine B, respectively, after 60 minutes of irradiation). This higher adsorption of dye molecules is attributed to the strong Lewis acidic Nb^{5+} on the surface and the big surface-to-volume ratio of Nb_2O_5 nanoplates (See Table S3 and Fig. S3, the surface areas are 31.7 cm^2/g and 5.3 cm^2/g for Nb_2O_5 nanoplates and commercial Nb_2O_5, respectively). It has been reported that Nb_2O_5 exhibits a different decomposition mechanism from the conventional radical-produced process. With regard to the strong adsorption of dye molecules, it seems that the dye molecules are immobilized at the solid acid sites, where the photoinduced electrons and holes on the surface can attack dye species without producing any radicals[32]. Therefore, the higher adsorbed amounts of dye molecules as well as the bigger surface-to-volume ratio of Nb_2O_5 nanoplates lead to the higher degree decomposition of dyes than commercial Nb_2O_5.

It has been reported that Nb_2O_5 is an efficient photocatalyst for the decomposition of indigo carmine, and almost 100% of dye decomposition occurs at 20, 45 and 90 minutes for TiO_2, ZnO and Nb_2O_5, respectively[57,58]. However, despite the fact that the as-prepared Nb_2O_5 nanoplates are reasonably efficient for the decomposition of dyes, the efficiency is not yet comparable to that of p25 (Fig. S4). The higher decomposition efficiency of p25 is due to its even larger surface-to-volume ratio (around 50 cm^2/g)[59–61], and rapid electron transfer between the mixed-phase of rutile and anatase[62]. The relationship between $\ln(c_0/c)$ and irradiation time (See Fig. S4b and S4d, c_0 and c are the concentrations of dyes in the solutions before and after irradiation) is not linear, suggesting that the decomposition of Methylene-blue and Rhodamine B does not follow pseudo-first-order kinetics of the Langmuir-Hinshelwood model. The convex function characterization of the as-prepared Nb_2O_5 nanoplates (Fig. S4b and S4d) may be ascribed to the self-accelerated effect due to the acidic intermediates produced during the composing process[41]. Further to that, it has also been reported that the decomposition of indigo carmine dye by Nb_2O_5 can be improved at lower pH values[57]. Because the decomposition of Methylene-blue molecules and Rhodamine B will produce carboxylic acid, NO_3^-, SO_4^{2-}, etc.[63,64], these intermediates may result in the slightly lower pH value of the solution. The above results indicate that the as-prepared Nb_2O_5 nanoplates have significantly better photocatalytic performances than commercial Nb_2O_5.

In summary, photodetectors based on Nb_2O_5 nanoplates have been fabricated and investigated. The Nb_2O_5 nanoplates are synthesized using a facile solvothermal method. On the one hand, the single Nb_2O_5 nanoplate photodetectors show remarkable sensitivity and wavelength selectivity with respect to UV-A light. They also exhibit robust stability and the generated photocurrent is substantially dependent on light intensity. On the other hand, good thermal stability is further observed of the Nb_2O_5 nanoplate films photodetector produced using the drop-casting method. In addition, the photocatalytic performance of the hexagonal-like Nb_2O_5 nanoplates in decomposing Methylene-blue and Rhodamine B dyes is significantly better than that of commercially purchased Nb_2O_5. These results considerably justify the potential of Nb_2O_5 nanoplates for high-performance UV-A photodetectors and photocatalyst.

Methods

The synthesis of Nb_2O_5 materials. In a typical synthesis of Nb_2O_5 nanoplates, a facile pre-hydrolysis reaction was conducted by adding $NbCl_5$ (0.27 g, 99.9%, Aladdin) and absolute ethanol (30 ml, > 95%, sinopharm) into deionized water (30 ml), which was subsequently kept for two hours at 25°C. After being stirred for another two hours, the aqueous suspension was immediately transferred into a Teflon lined autoclave (100 ml), and kept in oven at 250°C for 2 days. The white precipitate was collected using centrifugation, washed repeatedly with deionized water and ethanol several times, and dried at 60°C for five hours.

Device fabrication and characterization. For the fabrication of single hexagonal-like nanoplate photodetector, a droplet of Nb_2O_5 suspensions (2 mg of Nb_2O_5 powder dispersed in certain amounts of ethanol) was delivered gently on a thermally oxidized Si substrate covered with a 300 nm thick SiO_2 layer. The concentration of Nb_2O_5 suspensions were controlled carefully to ensure the sample dispersed on the substrate at a proper density (the nanoplates and nanorods were separated with a distance larger than the length of the interdigitated electrodes, which can be confirmed by optical microscope). Afterwards, the interdigitated electrodes (Ti/Au, 100/50 nm) were patterned on the top of nanoplates using photolithography, magnetron sputtering, and a carefully performed lift-off process. The finger was 10 μm wide and 390 μm long and the interspacing between the electrodes was 2 μm (Fig. S5). The interdigitated electrodes were patterned in arrays with 9 rows and 10 columns. Before current-voltage characterization, the location of the photodetector device based on single hexagonal-like nanoplate was confirmed by SEM. The current-voltage characteristics of the Nb_2O_5 nanoplate photodetectors were measured using an Advantest Picoammeter R8340A and a dc voltage source R6144. The spectral response for different wavelengths was triggered using a xenon lamp (500 W).

Materials characterization. The phase of as-obtained Nb_2O_5 nanoplates was identified by a Rigaku D/max-rB X-ray diffractometer using Cu Kα radiation (λ=0.15406 nm) in the 2θ range from 20° to 70°. The morphology characterization of the products was carried out by using field-emission scanning microscopy (FESEM, JEOL JSM-6701F) and transmission electron microscopy (TEM, JEOL JEM-2100F) equipped with an X-ray energy dispersive spectrometer (EDS). The UV-vis adsorption spectra were obtained using a Hitachi U-4100 spectrophotometer with the scanning wavelength from 700 nm to 200 nm. The XPS measurements were performed by a monochromatic Al Kα X-ray source (hv =1486.6 eV) with vacuum pressure of 1.0×10^{-9} Torr. Specific surface areas (BET) analysis was made using a Quantachrome instrument, and the software used was the Tristar 3000 v6.04.

Photocatalytic activity measurements. The photocatalytic activity of the as-prepared nanocrystals was evaluated by degrading Methylene-blue (dye content, ≥90%, Aladdin, (HPLC)), which is a dye resistant to biodegradation. The photocatalytic reactions were performed in a 50-ml Pyrex beaker at room temperature. For each run, 10 mg of powdered photocatalyst was added to 50 ml of Methylene-blue solution (2.5 mg/L) in deionized water, followed by a magnetic stir in the dark for 40 min to attain adsorption-desorption equilibrium. The beaker was then placed under a Hg arc lamp (Philips PL-S UV 100 W) positioned 20 cm above the base of the reaction vessel and illuminated during the entire photocatalytic reaction process. The slurry was continuously stirred to ensure full suspension of the nanocrystals throughout the reactions. 4 ml of solution mixtures was taken at given time intervals and centrifuged at 16500 rpm for 3 minutes prior to spectrometric analysis. UV-Vis absorption measurements were performed to analyze the degradation of Methylene-blue. The procedure of decomposition of Rhodamine B is the same as Methylene-blue, except the concentration of Rhodamine B and catalyst was changed to 15 mg/L and 30 mg, respectively.

1. Geim, A. K. & Novoselov, K. S. The rise of graphene. *Nat. Mater.* **6**, 183–191 (2007).
2. Gonokami, M. K. *et al.* Giant optical activity in quasi-two-dimensional planar nanostructures. *Phys. Rev. Lett.* **95**, 227401 (2005).
3. Li, Z. Q. & Zhang, Y. An efficient and user-friendly method for the synthesis of hexagonal-phase $NaYF_4$:Yb, Er/Tm nanocrystals with controllable shape and upconversion fluorescence. *Nanotechnology* **19**, 345606 (2008).
4. Zhang, Q. *et al.* Reconstruction of silver nanoplates by UV irradiation: tailored optical properties and enhanced stability. *Angew. Chem. Int. Ed.* **48**, 3516–3519 (2009).
5. Jang, E. S., Won, J. H., Hwang, S. J. & Choy, J. H. Fine tuning of the face orientation of ZnO crystals to optimize their photocatalytic activity. *Adv. Mater.* **18**, 3309–3312 (2006).
6. Seo, J. W. *et al.* Two-Dimensional SnS_2 nanoplates with extraordinary high discharge capacity for lithium ion batteries. *Adv. Mater.* **20**, 4269–4273 (2008).
7. Truong, Q. D., Devaraju, M. K., Ganbe, Y., Tomai, T. & Honma, I. Controlling the shape of $LiCoPO_4$ nanocrystals by supercritical fluid process for enhanced energy storage properties. *Sci. Rep.* **4**, 3975; DOI:3910.1038/srep03975 (2014).
8. Wu, Y. M., Wen, Z. H. & Li, J. H. Hierarchical carbon-coated $LiFePO_4$ nanoplate microspheres with high electrochemical performance for Li-ion batteries. *Adv. Mater.* **23**, 1126–1129 (2011).
9. Ye, X. C. *et al.* Competition of shape and interaction patchiness for self-assembling nanoplates. *Nat. Chem.* **5**, 466–473 (2013).
10. Ye, X. C. *et al.* Morphologically controlled synthesis of colloidal upconversion nanophosphors and their shape-directed self-assembly. *Proc. Natl. Acad. Sci. U. S. A.* **107**, 22430–22435 (2010).
11. Mehta, R. J. *et al.* A new class of doped nanobulk high-figure-of-merit thermoelectrics by scalable bottom-up assembly. *Nat. Mater.* **11**, 233–240 (2012).
12. Shi, W. D., Zhou, L., Song, S. Y., Yang, J. H. & Zhang, H. J. Hydrothermal synthesis and thermoelectric transport properties of impurity-free antimony telluride hexagonal nanoplates. *Adv. Mater.* **20**, 1892–1897 (2008).
13. Huang, Y. S., Zhang, Y. Z. & Hu, X. F. Structural, morphological and electrochromic properties of Nb_2O_5 films deposited by reactive sputtering. *Sol. Energy Mater. Sol. Cells* **77**, 155–162 (2003).
14. Rosenfeld, D. *et al.* Electrical transport properties of thin-film metal-oxide-metal Nb_2O_5 oxygen sensors. *Sensor Actuat B-Chem* **37**, 83–89 (1996).
15. Cantu, M. L., Norrman, K., Andreasen, J. W. & Krebs, F. C. Oxygen release and exchange in niobium oxide MEHPPV hybrid solar cells. *Chem. Mater.* **18**, 5684–5690 (2006).
16. Nakajima, K. *et al.* $Nb_2O_5.nH_2O$ as a heterogeneous catalyst with water-tolerant Lewis acid sites. *J. Am. Chem. Soc.* **133**, 4224–4227 (2011).
17. Žumer, M. *et al.* Field-emission properties of quasi-one-dimensional NbO_x crystals. *Appl. Phys. Lett.* **84**, 3615 (2004).
18. Mozetic, M., Cvelbar, U., Sunkara, M. K. & Vaddiraju, S. A method for the rapid synthesis of large quantities of metal oxide nanowires at low temperatures. *Adv. Mater.* **17**, 2138–2142 (2005).
19. Wei, M. D., Qi, Z. M., Ichihara, M. & Zhou, H. S. Synthesis of single-crystal niobium pentoxide nanobelts. *Acta Mater.* **56**, 2488–2494 (2008).
20. Li, L. H. *et al.* Phase evolution in low-dimensional niobium oxide synthesized by a topochemical method. *Inorg. Chem.* **49**, 1397–1403 (2010).
21. Yan, C. L. & Xue, D. F. Formation of Nb_2O_5 nanotube arrays through phase transformation. *Adv. Mater.* **20**, 1055–1058 (2008).
22. Wei, W., Lee, K., Shaw, S. & Schmuki, P. Anodic formation of high aspect ratio, self-ordered Nb_2O_5 nanotubes. *Chem. Commun.* **48**, 4244–4246 (2012).

23. Orilall, M. C., Abrams, N. M., Lee, J., DiSalvo, F. J. & Wiesner, U. Highly crystalline inverse opal transition metal oxides via a combined assembly of soft and hard chemistries. *J. Am. Chem. Soc.* **130**, 8882–8883 (2008).
24. Yang, P. D., Zhao, D. Y., Margolese, D. I., Chmelka, B. F. & Stucky, G. D. Generalized syntheses of large-pore mesoporous metal oxides with semicrystalline frameworks. *Nature* **396**, 152–155 (1998).
25. Nakajima, K. *et al.* Structure and acid catalysis of mesoporous $Nb_2O_5 \cdot nH_2O$. *Chem. Mater.* **22**, 3332–3339 (2010).
26. Li, L. H. *et al.* Niobium pentoxide hollow nanospheres with enhanced visible light photocatalytic activity. *J. Mater. Chem. A* **1**, 11894–11900 (2013).
27. Fan, W. Q., Zhang, Q. H., Deng, W. P. & Wang, Y. Niobic acid nanosheets synthesized by a simple hydrothermal method as efficient Brønsted acid catalysts. *Chem. Mater.* **25**, 3277–3287 (2013).
28. Lopes, O. F., Paris, E. C. & Ribeiro, C. Synthesis of Nb_2O_5 nanoparticles through the oxidant peroxide method applied to organic pollutant photodegradation: A mechanistic study. *Appl. Catal. B: Environ.* **144**, 800–808 (2014).
29. Varghese, B., Haur, S. C. & Lim, C. T. Nb_2O_5 nanowires as efficient electron field emitters. *J. Phys. Chem. C* **112**, 10008–10012 (2008).
30. Wei, M. D., Wei, K. M., Ichihara, M. & Zhou, H. S. Nb_2O_5 nanobelts: A lithium intercalation host with large capacity and high rate capability. *Electrochem. Commun.* **10**, 980–983 (2008).
31. Fang, X. S. *et al.* New ultraviolet photodetector based on individual Nb_2O_5 nanobelts. *Adv. Funct. Mater.* **21**, 3907–3915 (2011).
32. Zhao, Y. *et al.* Shape-dependent acidity and photocatalytic activity of Nb_2O_5 nanocrystals with an active TT (001) surface. *Angew. Chem. Int. Ed.* **51**, 3846–3849 (2012).
33. Xu, X. *et al.* Ordered mesoporous niobium oxide film: A novel matrix for assembling functional proteins for bioelectrochemical applications. *Adv. Mater.* **15**, 1932–1936 (2003).
34. Wang, Z. *et al.* Fast and highly-sensitive hydrogen sensing of Nb_2O_5 nanowires at room temperature. *Int. J. Hydrogen Energy* **37**, 4526–4532 (2012).
35. Özer, N., Chen, D. G. & Lampert, C. M. Preparation and properties of spin-coated Nb_2O_5 films by the sol-gel process for electrochromic applications. *Thin Solid Films* **277**, 162–168 (1996).
36. Yoshimura, K., Miki, T., Iwama, S. & Tanemura, S. Characterization of niobium oxide electrochromic thin films prepared by reactive dc magnetron sputtering. *Thin Solid Films* **281**, 235–238 (1996).
37. Zhou, Y. Y., Qiu, Z. F., Lü, M. K., Zhang, A. Y. & Ma, Q. Preparation and spectroscopic properties of Nb_2O_5 nanorods. *J. Lumin.* **128**, 1369–1372 (2008).
38. Fang, X. S. *et al.* ZnO and ZnS nanostructures: ultraviolet-light emitters, lasers, and sensors. *Crit. Rev. Solid State Mater. Sci.* **34**, 190–223 (2009).
39. Fang, X. S. *et al.* Single-crystalline ZnS nanobelts as ultraviolet-light sensors. *Adv. Mater.* **21**, 2034–2039 (2009).
40. Hu, L. F., Yan, J., Liao, M. Y., Wu, L. M. & Fang, X. S. Ultrahigh external quantum efficiency from thin SnO_2 nanowire ultraviolet photodetectors. *Small* **7**, 1012–1017 (2011).
41. Li, W., Gao, R., Chen, M., Zhou, S. X. & Wu, L. M. Facile synthesis and unique photocatalytic property of niobium pentoxide hollow spheres and the high optoelectronic performance of their nanofilm. *J. Colloid Interface Sci.* **411**, 220–229 (2013).
42. Tamang, R., Varghese, B., Mhaisalkar, S. G., Tok, E. S. & Sow, C. H. Probing the photoresponse of individual Nb_2O_5 nanowires with global and localized laser beam irradiation. *Nanotechnology* **22**, 115202 (2011).
43. Gao, B. *et al.* Quasi-aligned Ag-Nb_2O_5 nanobelt arrays with enhanced photocatalytic and antibacterial activities. *J. Am. Ceram. Soc.* **94**, 2330–2338 (2011).
44. Zhang, Z. Y., Jin, C. H., Liang, X. L., Chen, Q. & Peng, L. M. Current-voltage characteristics and parameter retrieval of semiconducting nanowires. *Appl. Phys. Lett.* **88**, 073102 (2006).
45. Zhang, Z. Y. *et al.* Quantitative analysis of current-voltage characteristics of semiconducting nanowires: Decoupling of contact effects. *Adv. Funct. Mater.* **17**, 2478–2489 (2007).
46. Salvador, P. Analysis of the physical properties of TiO_2 be electrodes in the photoassisted oxidation of water. *Sol. Energy Mater.* **6**, 241–250 (1982).
47. Fang, X. S., Bando, Y., Ye, C. H., Shen, G. Z. & Golberg, D. Shape-and size-controlled growth of ZnS nanostructures. *J. Phys. Chem. C.* **111**, 8469–8474 (2007).
48. Li, L. *et al.* Electrical transport and high-performance photoconductivity in individual ZrS_2 nanobelts. *Adv. Mater.* **22**, 4151–4156 (2010).
49. Mihailetchi, V., Wildeman, J. & Blom, P. Space-Charge Limited Photocurrent. *Phys. Rev. Lett.* **94**, 126602 (2005).
50. Pfüller, C. *et al.* Unpinning the Fermi level of GaN nanowires by ultraviolet radiation. *Phys. Rev. B* **82**, 045320 (2010).
51. Posada, F. G., Songmuang, R., Hertog, M. D. & Monroy, E. Room-temperature photodetection dynamics of single GaN nanowires. *Nano Lett.* **12**, 172–178 (2012).
52. Hertog, M. I. *et al.* Correlation of polarity and crystal structure with optoelectronic and transport properties of GaN/AlN/GaN nanowire sensors. *Nano Lett.* **12**, 5691–5697 (2012).
53. Soci, C. *et al.* ZnO nanowire UV photodetectors with high internal gain. *Nano Lett.* **7**, 1003–1009 (2007).
54. Iskandar, F. *et al.* Enhanced photocatalytic performance of brookite TiO_2 macroporous particles prepared by spray drying with colloidal templating. *Adv. Mater.* **19**, 1408–1412 (2007).
55. Hu, X. F., Mohamood, T., Ma, W. H., Chen, C. C. & Zhao, J. C. Oxidative decomposition of rhodamine B dye in the presence of VO^{2+} and/or Pt(IV) under visible light irradiation: N-deethylation, chromophore cleavage, and mineralization. *J. Phys. Chem. B* **110**, 26012–26018 (2006).
56. Chen, F., Zhao, J. C. & Hidaka, H. Highly selective deethylation of rhodamine B: Adsorption and photooxidation pathways of the dye on the TiO_2/SiO_2 composite photocatalyst. *Int. J. Photoenergy.* **5**, 209–217 (2003).
57. Prado, A. G. S., Bolzon, L. B., Pedroso, C. P., Moura, A. O. & Costa, L. L. Nb_2O_5 as efficient and recyclable photocatalyst for indigo carmine degradation. *Appl. Catal. B: Environ.* **82**, 219–224 (2008).
58. Qi, S., Zuo, R., Liu, Y. & Wang, Y. Synthesis and photocatalytic activity of electrospun niobium oxide nanofibers. *Mater. Res. Bull.* **48**, 1213–1217 (2013).
59. Suttiponparnit, K. *et al.* Role of surface area, primary particle size, and crystal phase on titanium dioxide nanoparticle dispersion properties. *Nanoscale Res. Lett.* **6**, 1–8 (2011).
60. Raj, K. J. A. & Viswanathan, B. Effect of surface area, pore volume and particle size of P25 titania on the phase transformation of anatase to rutile. *Indian J. Chem. A* **48**, 1378 (2009).
61. Tian, G., Fu, H., Jing, L., Xin, B. & Pan, K. Preparation and characterization of stable biphase TiO_2 photocatalyst with high crystallinity, large surface area, and enhanced photoactivity. *J. Phys. Chem. C.* **112**, 3083–3089 (2008).
62. Hurum, D. C., Agrios, A. G., Gray, K. A., Rajh, T. & Thurnauer, M. C. Explaining the enhanced photocatalytic activity of Degussa P25 mixed-phase TiO_2 using EPR. *J. Phys. Chem. B* **107**, 4545–4549 (2003).
63. Houas, A. *et al.* Photocatalytic degradation pathway of methylene blue in water. *Appl. Catal. B: Environ.* **31**, 145–157 (2001).
64. Lachheb, H. *et al.* Photocatalytic degradation of various types of dyes (Alizarin S., Crocein Orange G., Methyl Red, Congo Red, Methylene Blue) in water by UV-irradiated titania. *Appl. Catal. B: Environ.* **39**, 75–90 (2002).

Acknowledgments

We thank Prof. Linfeng Hu from Fudan University and Dr. W. Tian from National Institute for Materials Science (NIMS) for for valuable discussions and the HRTEM measurements, respectively. This work was supported by the National Natural Science Foundation of China (Grant No 51471051), the Project of Short-Term International Visiting for PhD Candidates at Fudan University (2013), Shanghai Shu Guang Project (12SG01), Science and Technology Commission of Shanghai Municipality (13NM1400300), the Programs for Professor of Special Appointment (Eastern Scholar) at Shanghai Institutions of Higher Learning and for New Century Excellent Talents in University (NCET-11-0102).

Author contributions

L.H. and F.X.S. supervised the project, conceived the experiments, analyzed the results and wrote the paper. G.N. helped for the linguistic polish. L.M.Y. helped with collected and analysis the data. All authors participated in analysis and discusion the results and commented on the manuscript.

Additional information

Supplementary information accompanies this paper at http://www.nature.com/scientificreports

Competing financial interests: The authors declare no competing financial interests.

How to cite this article: Liu, H., Gao, N., Liao, M. & Fang, X. Hexagonal-like Nb_2O_5 Nanoplates-Based Photodetectors and Photocatalyst with High Performances. *Sci. Rep.* **5**, 7716; DOI:10.1038/srep07716 (2015).